Progress In Electromagnetics Research, Vol. 147, 69–79, 2014

Light Absorber with an Ultra-Broad Flat Band Based on Multi-Sized Slow-Wave Hyperbolic Metamaterial Thin-Films

Sailing He$^{1, 2, 3, *}$, Fei Ding^{1}, Lei Mo$^{1, 4}$, and Fanglin Bao$^{1, 2, 4}$

(*Invited Paper*)

Abstract—Here we realize a broadband absorber by using a hyperbolic metamaterial composed of alternating aluminum-alumina thin films based on superposition of multiple slow-wave modes. Our super absorber ensures broadband and polarization-insensitive light absorption over almost the entire solar spectrum, near-infrared and short-wavelength infrared regime (500–2500 nm) with a simulated absorption of over 90%. The designed structure is fabricated and the measured results are given. This absorber yields an average measured absorption of 85% in the spectrum ranging from 500 nm to 2300 nm. The proposed absorbers open an avenue towards realizing thermal emission and energy-harvesting materials.

1. INTRODUCTION

Metamaterials are attractive for not only their special electromagnetic properties, but also their potential for new effects and devices, such as negative refraction, cloaking, super-lenses and absorbers. Recent studies have focused on some metamaterial perfect absorbers, which can achieve near-unity absorption of electromagnetic waves and enhance the performance of thermal emitters and thermo-photovoltaic systems. Perfect electromagnetic (EM) wave absorbers, which can completely absorb all incident EM radiation without producing any reflection, transmission or scattering [1], are of increasing importance in many fields of science and engineering, e.g., thermal emitters and collection of solar energy. Thin film perfect absorbers, which can effectively trap photons and transfer their energy into electrical or thermal energy within a few hundred nanometers, are of particular interest, playing an important role in thermo-photovoltaic systems and thermoelectric generators [1–3]. However, such thin film absorbers are extremely difficult to create because there do not exist many natural materials that can absorb EM radiation over a wide wavelength range and for a wide range of incident angles.

A possible route to realizing efficient light absorption is to use various plasmonic structures, including micro-cavities [4], strips [5–7] and subwavelength slits [8, 9]. Metamaterials (MMs) are also promising candidates for designing stable thin film perfect absorbers, exhibiting wavelength scalability as well as angle or polarization insensitivity [10–13]. However, due to the resonant nature, the aforementioned absorbers often tend to be narrow banded, limiting practical applications. An effective method to extend the absorption bandwidth is to blend together various strong resonators operating at several neighboring frequencies [14–18]. However, the bandwidth of the absorption spectrum cannot be broadened significantly because the number of resonators is limited.

Received 3 April 2014, Accepted 22 May 2014, Scheduled 15 June 2014

* Corresponding author: Sailing He (sailing@jorcep.org).

[1] Centre for Optical and Electromagnetic Research, Zhejiang Provincial Key Laboratory for Sensing Technologies, JORCEP, Zhejiang University, Hangzhou 310058, China. [2] ZJU-SCNU Joint Research Center of Photonics, Centre for Optical and Electromagnetic Research, South China Academy of Advanced Optoelectronics, South China Normal University (SCNU), Guangzhou 510006, China. [3] Department of Electromagnetic Engineering, School of Electrical Engineering, Royal Institute of Technology, Stockholm S-100 44, Sweden. [4] Department of Physics, Zhejiang University, Hangzhou 310058, China. Sailing He and Fei Ding contributed equally.

Recently, non-resonant thin film absorbers have been demonstrated with composite metamaterials involving metal nanoparticles embedded in dielectric layers [19, 20]. When the antireflection effect of a tapered subwavelength strip is introduced, a tungsten slab consisting of pyramid arrays can theoretically display nearly-complete absorption throughout the entire solar spectrum [21]. Based on adiabatic nanofocusing of gap surface plasmon modes excited by the scattering off subwavelength-sized wedges, broadband visible light absorption can be realized in ultra-sharp convex metal grooves [22]. Non-resonant absorption by tungsten pyramid arrays and ultra-sharp convex metal grooves is broadband, but the designed structures are too sophisticated to demonstrate and the absorption performance is not robust, with minor experimental deviations. Additionally, the ultra-sharp convex metal grooves have a long wavelength limit due to both the adiabatic condition and the decrease in the plasmon absorption for longer wavelengths [22]. At the same time, a sawtoothed anisotropic metamaterials slab, which can effectively excite slow-wave modes, has been shown to achieve a large bandwidth of about 86% of its central wavelength [23] (experimental verification has been done in the microwave regime [24]).

In this paper, we realized ultra-broadband absorbers, which can cover the visible and near-infrared regime by patterning multi-sized hyperbolic metamaterial (HMM) cells with appropriate geometrical parameters in a co-plane. We demonstrate experimentally that a two-dimensional (2D) quadrangular frustum pyramid (QFP) absorber in the wavelength range from 500 nm to 2300 nm. Moreover, the absorption is polarization insensitive due to the symmetry arrangement of the QFP absorber design.

2. RESULTS

2.1. Polarization-Dependent Absorption in Tapered Strip Array

Firstly, we investigate a structure consisting of alternating thin Alumina (Al_2O_3) and Aluminum (Al) films. The permittivity and thickness of the Al_2O_3 layers are ε_d and t_d, respectively, and ε_m and t_m for the Al layers. When the thickness of each layer is much smaller than the wavelength, the periodic structure can be homogenized as an MM with effective anisotropic permittivity ε_{mm}. According to the effective medium theory [25], the permittivity tensor ε_{mm} can be approximately written as

$$\begin{aligned}\varepsilon_x = \varepsilon_y &= f \cdot \varepsilon_m + (1-f) \cdot \varepsilon_d \\ \varepsilon_z &= \frac{\varepsilon_m \cdot \varepsilon_d}{f \cdot \varepsilon_d + (1-f) \cdot \varepsilon_m}\end{aligned} \tag{1}$$

where $f = t_m/(t_m + t_d)$ is the filling ratio of the metal. Firstly, 20 pairs of Al_2O_3-Al layers are used to construct the practical structure with $t_d = 8\,\text{nm}$, $t_m = 12\,\text{nm}$ and $f = 0.6$ (Figure 1(a)). Considering the dispersive permittivities of Al_2O_3 and Al (Ref. [26]), we see $\text{Re}(\varepsilon_x) < 0$ and $\text{Re}(\varepsilon_z) > 0$, and this multilayered MM is a hyperbolic MM (HMM) whose equal-frequency dispersion curve is hyperbolic throughout the visible, near-infrared, and mid-infrared spectral regions. For instance, the real and imaginary parts of ε_{mm} calculated with Eq. (1) are plotted in Figure 1(b), verifying the HMM condition.

Then, we carved this HMM slab into periodic tapered strips with period $P_x = 300\,\text{nm}$, top width $W_t = 50\,\text{nm}$ and bottom width $W_b = 300\,\text{nm}$, which can realize broadband strong absorbers based on the slow-wave effect, as illustrated in Figure 1(a). The HMM tapered strip array is constructed on an Au film with a thickness (100 nm) large enough to block light transmission.

We performed full wave electromagnetic simulations using the finite difference time domain (FDTD) method and finite element method (FEM). In the simulations, a periodic boundary condition is used in the x direction, and a plane wave of TM polarization is incident downwards along the z direction as an excitation source, which means that the incident plane is the x-z plane and the magnetic field is polarized along the y axis. The absorption is defined by $A(\omega) = 1 - T(\omega) - R(\omega)$, where $T(\omega)$ and $R(\omega)$ are the total transmission and reflection. Since the bottom gold film is thick enough, the transmission equals zero for the entire investigated spectrum, and consequently the absorption can be given simply by $A(\omega) = 1 - R(\omega)$.

The obtained absorption spectrum at normal incidence (black dashed-dotted in Figure 1(c)) indicates that the absorption performance is excellent, with absorptivity higher than 90% covering the wavelength range from 500 nm to 1850 nm. We find that the absorption obtained from the practical multilayered tapered strip array with 20 Al_2O_3-Al pairs (black dashed-dotted in Figure 1(c)) is almost

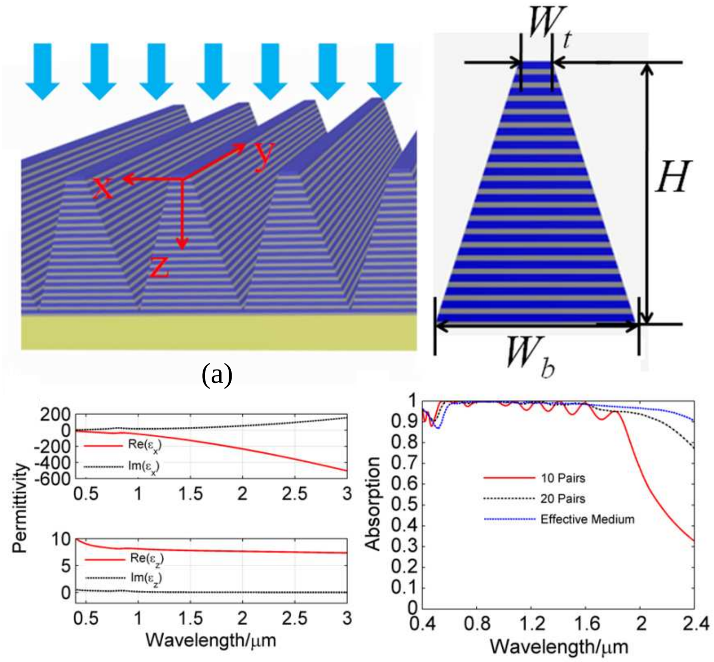

(a)

(b)

(c)

Figure 1. (a) Schematic of the 1D HMM absorber with 20 Al_2O_3-Al pairs. $W_t = 50\,\text{nm}$, $W_b = 300\,\text{nm}$, $P_x = 300\,\text{nm}$ and $H = 400\,\text{nm}$. (b) Components of ε_{mm} calculated using Eq. (1). (c) Absorption spectra for the multilayered absorber with 10 Al_2O_3-Al pairs (red solid line), 20 Al_2O_3-Al pairs (black dashed line) and the effective homogeneous structure (blue dash-dotted line).

the same as that of the homogenous effective HMM absorber (blue dash-dotted line in Figure 1(c)), which indicates that the effective medium theory is valid for the present case.

If we discretize the homogenous effective pyramid into Al_2O_3-Al composite layers by a smaller number of pairs than the present case, e.g., 10 pairs, while the height of the tapered strip array and the filling ratio are fixed ($H = 400\,\text{nm}$, $t_d = 16\,\text{nm}$ and $t_m = 24\,\text{nm}$), the calculated spectrum (red solid line in Figure 1(c)) of the discrete model is very close to those of the 20-pair practical absorber and effective homogeneous HMM absorber except for some oscillations. This is because in this case the thickness (t_m) of the Al plates is close to the skin depth of Al within the studied wavelength range so that the incident light cannot penetrate through the metal directly. Although there are some small oscillations, the strong absorption is still maintained, and this absorber consisting of 10 Al_2O_3-Al pairs is much easier to fabricate.

As stated in Ref. [23], the broadband absorption arises from a slow-wave effect supported by the HMM tapered strip array. The HMM tapered strips can be treated as periodic tapered waveguides. For a guided mode at some wavelengths, when it propagates down along an MM-tapered waveguide gradually towards some critical width where the group velocity ($v_g = d\omega_c/d\beta$) approaches 0, it is slowed down, trapped, and blocked. Due to the specific gradient shape, these waveguides can achieve a broadband and tunable slow-wave effect. As the tapered waveguides are lossy, the energy of the supported guided modes is strongly absorbed. Thus the incident light can be efficiently absorbed in a wide, long-wavelength range.

To better understand this absorbing mechanism, the magnetic field distributions for the practical multilayered tapered strips (20 pairs of Al_2O_3-Al layers) at several different wavelengths ($\lambda = 0.8\,\mu\text{m}$, $1.2\,\mu\text{m}$, and $1.6\,\mu\text{m}$) are respectively shown in Figures 2(a)–(c), and the corresponding magnetic field distributions for the homogenous effective tapered strips are displayed in Figures 2(d)–(f).

It is obvious that the practical strips and homogenous structure have very similar field distributions except for some details around Al_2O_3-Al interfaces due to the average effect of the effective medium theory. In the practical structure, the resonant magnetic field is not just localized in the dielectric

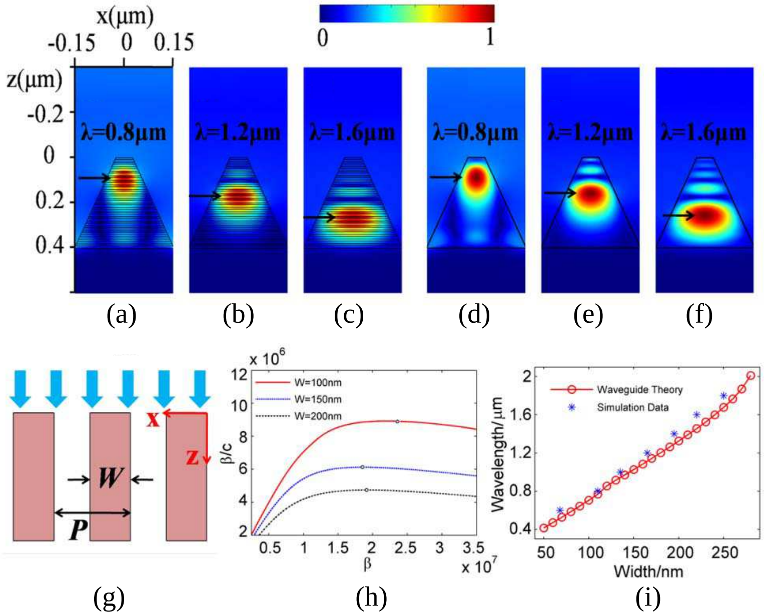

Figure 2. (a)–(c) Magnetic field amplitude distributions at different incident wavelengths for the practical absorber of 20 Al_2O_3-Al pairs. (d)–(f) Corresponding magnetic field amplitude distributions at different incident wavelengths for the effective homogeneous structure. (g) Schematic of periodic air/HMM/air waveguide array with a fixed core width of W and period of P. Only three cells are shown. (h) Dispersion curves of the periodic air/HMM/air waveguide array at different W. Black circle points show degeneracy points. (i) The cutoff wavelength at different widths from the waveguide theory (red solid line with circles) and simulation data (blue star points).

spacer between two neighboring metal layers, but diffuses into several dielectric spacers. It is seen that the incident light at a certain wavelength accumulates at a certain position of the tapered strips. For instance, the incident light at $\lambda = 0.8\,\mu m$ is trapped mainly at the upper part of the strip, and the magnetic fields at the bottom part are weak. The incident light at $\lambda = 1.2\,\mu m$ is localized at the middle waist region. At a longer wavelength, $\lambda = 1.6\,\mu m$, the incident light is mainly harvested by the bottom part, whereas around the top parts there is almost no strong field concentration.

To further demonstrate the slow-wave nature of the guided modes in the tapered hyperbolic waveguides, we calculated the dispersion curves of a periodic hyperbolic waveguide array with a fixed core width (Figure 2(g)). In the hyperbolic waveguide array, the guided modes in adjacent waveguides will couple and interact with each other due to the overlap of evanescent fields. Therefore, we should take the period into consideration. Based on Maxwell's equations and boundary conditions (Ref. [27]), the dispersion relationship between the incident photon frequency ($\omega_c = \omega/c$) and the propagating constant (β) is derived as

$$\tan\left(k_x \cdot \frac{W}{2}\right) - \frac{k_1}{k_x}\varepsilon_z \cdot \tanh\left[k_1 \cdot \frac{P-W}{2}\right] = 0 \tag{2}$$

where $k_x = \sqrt{\omega_c^2\varepsilon_z - \frac{\varepsilon_z}{\varepsilon_x} \cdot \beta^2}$, $k_1 = \sqrt{\beta^2 - \omega_c^2}$, P is the period and W is the core width of the waveguide. In this calculation, the structures are supposed to be lossless for simplicity. When $P = 300\,\text{nm}$, for $W = 100\,\text{nm}$, $W = 150\,\text{nm}$, and $W = 200\,\text{nm}$, the dispersion curves of the fundamental mode are plotted in Figure 2(h). One can see that the propagating constant increases gradually with the frequency at first; then the incident light approaches the cutoff frequency where the degeneracy point occurs; after the cutoff frequency, the dispersion line declines slightly. At the degeneracy points ($\lambda = 0.704\,\mu m$, $1.026\,\mu m$ and $1.325\,\mu m$), v_g approaches zero, indicated by the black empty circles. Therefore, for a waveguide of a certain core width, the slow-wave modes can be excited around a certain wavelength. Though the lossless assumption cannot explain the physics of broadband absorption accurately, the degeneracy points at the dispersion curves of lossless structures can approximately predict the critical width [28, 29].

We also plotted the cutoff wavelength at different widths in Figure 2(i). In Figure 2(i), one can see that the air/HMM/air waveguide of widths from 50 to 280 nm can support slow light modes of wavelengths from 0.4 µm to 2 µm, which is in good agreement with the absorption band shown in Figure 1(c). Additionally, for a certain width, the corresponding cutoff wavelengths calculated from simulation data (blue star points) and the dispersion curves of waveguide theory (red solid line with circles) are essentially consistent.

2.2. Tune and Broaden the Absorption Spectrum

For this multilayered structure composed of alternating Al_2O_3-Al layers, the HMM condition ($\mathrm{Re}(\varepsilon_x) < 0$ and $\mathrm{Re}(\varepsilon_z) > 0$) is fulfilled throughout the visible, near-infrared and mid-infrared spectral regions. Therefore a broadband and tunable slow-wave effect can be fulfilled. In addition the absorption spectrum of the proposed absorber is flexible and can be easily tuned with proper design.

As mentioned above, there is a one-to-one correspondence between the wavelength of incident light and the width of the HMM strip (different positions of the tapered strip), which means that a wider strip can accommodate light with a longer wavelength. If we enlarge the tapered strip, we can achieve a perfect absorber working in the longer wavelength range. For example, we take the HMM made up of 10 Al_2O_3-Al pairs into consideration. During the optimization, the height of the tapered strips and the filling ratio are kept constant ($H = 400\,\mathrm{nm}$, $t_d = 16\,\mathrm{nm}$ and $t_m = 24\,\mathrm{nm}$). As shown in Figure 3(a), a larger tapered strip with period $P_x = 550\,\mathrm{nm}$, top width $W_t = 150\,\mathrm{nm}$ and bottom width $W_b = 500\,\mathrm{nm}$ can achieve perfect absorption from 1400 nm to 2800 nm, with over 90% light absorbed in this spectrum, revealing the flexibility and scalability of this absorber.

Below we try to increase the bandwidth of the absorption by assembling multi-sized tapered strips with appropriate geometrical parameters in a co-planar. As mentioned above, the working absorption spectrum will vary with the variation of geometrical parameters. Therefore, multi-sized strips with different geometrical parameters are positioned on a co-planar to ensure that the absorption frequencies can be close to each other, giving a broader absorption spectrum.

For the sake of simplicity and clarity, we study the case of two different-sized tapered strip arrays (i.e., pyramids) made of 10 Al_2O_3-Al pairs placed in a unit cell with a fixed total height and metal filling ratio. Firstly we just put the two aforementioned different-sized pyramids into a unit cell. The top and bottom widths of the large pyramid are $W_{t1} = 150\,\mathrm{nm}$ and $W_{b1} = 500\,\mathrm{nm}$, respectively, and $W_{t2} = 50\,\mathrm{nm}$ and $W_{b2} = 300\,\mathrm{nm}$ for the small pyramid. As shown in Figure 3(b) (black dashed line), the absorber with two sub-cells can achieve a broader absorption spectrum. However, the absorption performance is still far from satisfactory as the absorption efficiency is not very high in the visible frequency regime

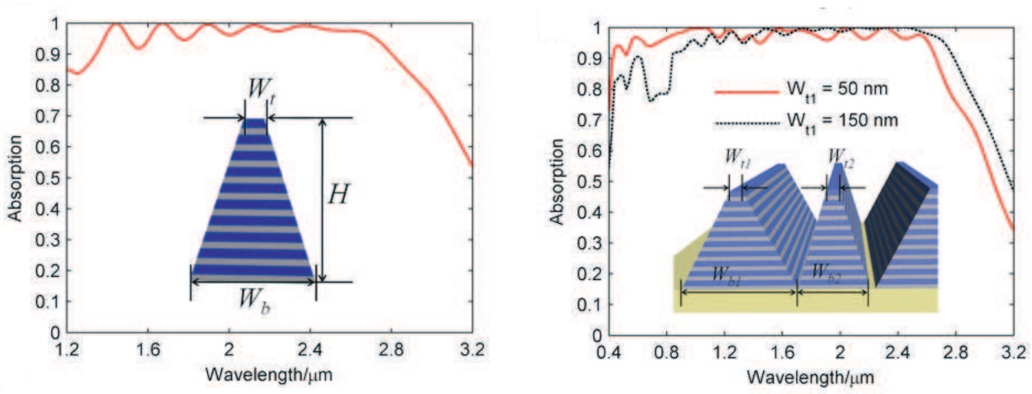

(a) (b)

Figure 3. (a) Schematic of the 1D strip absorber with 10 Al_2O_3-Al pairs. $W_t = 150\,\mathrm{nm}$, $W_b = 500\,\mathrm{nm}$, and $P_x = 550\,\mathrm{nm}$. (b) Absorption spectra for broadband absorber consisting of two different sized sub-cells with different top widths. $W_{t2} = 50\,\mathrm{nm}$, $W_{b1} = 500\,\mathrm{nm}$, $W_{b2} = 300\,\mathrm{nm}$, and $P_x = 825\,\mathrm{nm}$.

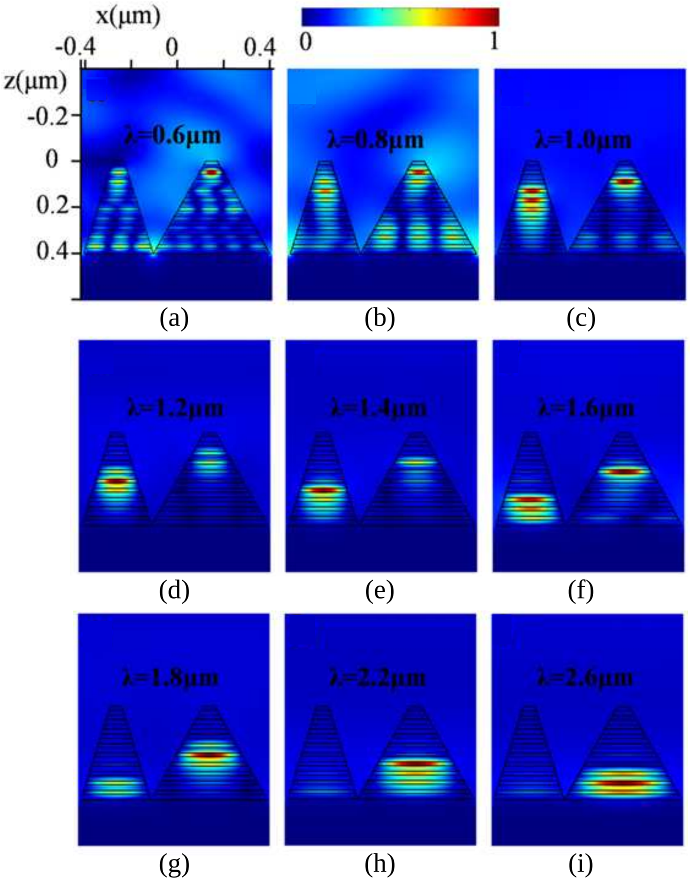

Figure 4. (a)–(i) Magnetic field amplitude distributions at different incident wavelengths for a broadband absorber consisting of two different sized sub-cells within a unit cell. The parameters are $W_{t1} = W_{t2} = 50\,\text{nm}$, $W_{b1} = 500\,\text{nm}$, $W_{b2} = 300\,\text{nm}$, $P_x = 825\,\text{nm}$.

and there are dips around 800 nm. This trend is understandable. When two pyramids are put together into a unit cell, the effective absorption cross-section of the incident light in the short wavelength range declines noticeably, and more light will transmit directly through the gaps between neighboring HMM strips down to the gold film and be finally reflected. To overcome this problem and simplify the design, we only decrease the top width of the large pyramid (W_{t1}) to increase the absorption cross-section for the short wavelength light, improving the absorption efficiency in short wavelength range. A quite good result is obtained when W_{t1} is reduced to 50 nm and other parameters are kept unchanged. As shown in Figure 3(b) (red solid line), more than 90% of light is absorbed from 500 nm to 2500 nm, and the full absorption bandwidth at half maximum (FWHM) is above 150%, which is much wider than that in the previous cases.

To verify the physical insight better, we calculate the magnetic field distributions at some wavelengths of the absorber within a unit cell, depicted in Figure 4. When the wavelength is small, as shown in Figure 4(a)–(c), both the small and large pyramids contribute to the absorption. In other words, light is not solely accumulated at a certain part of one type of pyramid, but rather is trapped at multiple regions within both pyramids. In addition both the fundamental and high order slow-wave modes are generated. When the wavelength gets larger but below 1.6 μm (Figures 4(d)–(f)), light is mainly concentrated in the small pyramid, and the light with the longer wavelength will stay in the wider part of the pyramid. At $\lambda = 1.6\,\mu\text{m}$, the small pyramid cannot accommodate the slow-wave mode independently, and thus some energy transfer is stored in the large pyramid (Figure 4(f)). In the wavelength range above 1.8 μm, the large pyramid dominates the light absorption and nearly all the energy is trapped and absorbed in it. Analogously, light of differing wavelengths is strongly trapped at some part of the large pyramid corresponding to the specific width of the strip.

2.3. Experimental Results

In the above, the 1D tapered strip absorber is polarization dependent. To remove this polarization-dependence, a two-dimensional (2D) periodic array of quadrangular frustum pyramids (QFPs) is proposed, and is illustrated in Figure 5(a). The parameters of QFPs are identical to those of the 1D multi-sized strip array, and the period along the y direction is the same as that along the x direction.

To experimentally observe the broadband absorption, we have fabricated the 2D QFP absorber ($15\,\mu\text{m} \times 15\,\mu\text{m}$) via thin-film deposition combined with focused-ion-beam (FIB) milling. The 10 pairs of alternating Al_2O_3-Al thin films are firstly deposited on the Au-film-coated silicon substrate with sputtering. Then FIB milling is used to pattern the 1D tapered strip arrays. During the milling, a proper grayscale bitmap is designed to distribute the dose intensity, which can control the tapered angle. The scanning electron microscopy (SEM) image of the fabricated parallel strips along the x-axis is shown in Figure 5(b). When this 1D tapered strip array along the x direction is fabricated, an orthogonal strip array along the y direction is milled to construct the 2D QFP absorber. This process is vital for realizing the symmetry absorber, which is polarization-independent. In reality, the process is really strenuous as some milled away materials may get into the pre-fabricated grooves along the x direction when milling the crossed strips along the y direction, which will lead to strong geometric asymmetry. After trying several times with different grayscale bitmaps and doses, we have successfully implemented a 2D QFP absorber with acceptable structural asymmetry, illustrated in Figure 5(c).

As the absorption bandwidth is wide, the total reflection $R(\omega)$ is measured separately with two different setups. In the wavelength range of 500 nm–1650 nm, we use makeshift linear reflection spectroscopy to measure the reflection, based on an inverted microscope equipped with a super-continuum source, pinholes and spectrometers. Thus the measured spectral range is limited by the response of spectrometers. That is why there is a gap between 900 nm and 1000 nm. In the wavelength range over 1600 nm, we adopt another detection system based on a monochromator.

The measured absorption spectrum is broad and flat except for some oscillations around 2300 nm,

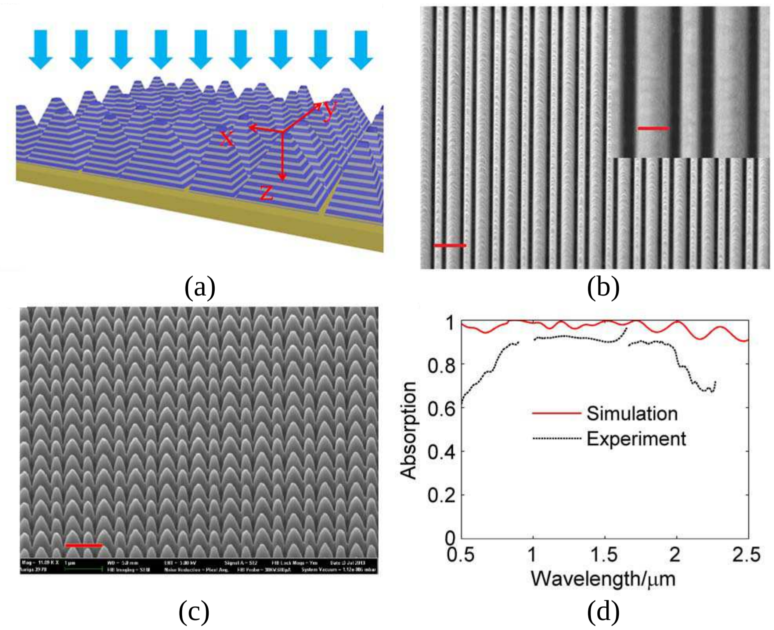

(a) (b)

(c) (d)

Figure 5. (a) Schematic of the simulated 2D QFP absorber; the parameters of a unit cell are $W_{t1} = W_{t2} = 50\,\text{nm}$, $W_{b1} = 500\,\text{nm}$, $W_{b2} = 300\,\text{nm}$, $P_x = P_y = 825\,\text{nm}$, $t_m = 24\,\text{nm}$, $t_d = 16\,\text{nm}$. (b) SEM images of 1D taper array along the y axis (scale bar 1 µm) milled in a multilayered film displaying slight period variations and surface roughness (see inset, scale bar 300 nm). (c) SEM images of 2D QFP arrays. (d) Comparison between the experimental absorption (black dashed line) and simulated absorption (red solid line). The normally incident light is arbitrarily polarized.

and the absorption is above 0.8 from 730 nm to 2010 nm. On average, the measured absorption at normal incidence between 500 nm and 2300 nm is found to be 0.85 for arbitrary polarized light [see dashed black curve in Figure 5(d)]. The experimental data is in good agreement with the simulated spectrum in the middle wavelength range (1000 nm–2000 nm), considering the imperfection in the fabricating process as well as the measurement error. However, the discrepancy between the curves in the short wavelength range (500 nm–700 nm) is a little bit big, which is ascribed to the variation of the parameters of the fabricated QFP absorber from those of the designed structure. As the top layer of QFP is only 50 nm wide, in the fabrication process, it will deviate from the designed shape, becoming a tip. Then the light in the short wavelength cannot be efficiently trapped and will be reflected. Therefore the absorption efficiency in the short wavelength range is not high. In addition, the low absorption in the long wavelength range (2000 nm–2300 nm) is ascribed to another factor besides the imperfection fabrication. As the lenses in our system are made up of BK7 glass and have a relatively strong absorption at long wavelengths, it brings the signals into a dramatic dissipation. Then we have to tune up the pinhole area to get an acceptable signal-to-noise ratio, meanwhile, more reflecting lights from the vicinity of the structure are collected somehow, reducing the measured absorption coefficient.

2.4. Angle-Independent Absorption Performance

Ideally, the performance of the absorber should be insensitive to the incident angle (θ) for applications such as solar energy harvesting. We performed the full-wave simulations to verify the angle dispersion for both TE polarization (the electric field of the incident light is kept parallel to the y-axis, Figure 6(a)) and TM polarization (the magnetic field of the incident light is kept parallel to the y-axis, Figure 6(b)) and found that the absorption effect is nearly robust for oblique incidence. In the simulation, the incident angle (θ) is varied in 5° steps from 0° to 80°. For both polarizations, the absorption is nearly independent of the incident angle (θ), and the broadband response is achieved when the angle is below 40°. In addition, the absorption still remains above 80% even when the incident angle reaches 60°.

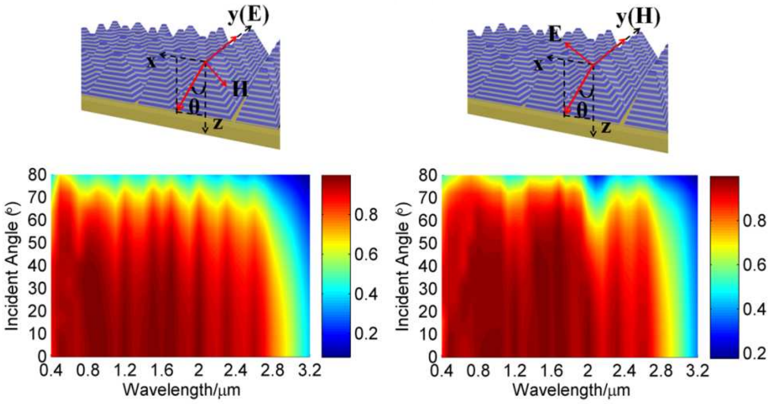

(a) (b)

Figure 6. Incident angle dependence of the absorption performance. (a) Absorption as a function of the wavelength and incident angle for TE polarization. (b) Absorption as a function of the wavelength and incident angle for TM polarization.

3. CONCLUSIONS

We have successfully realized ultra-broadband absorbers based on multi-sized HMM slow-wave structures, which ensures polarization-insensitive light absorption (above 90%) between 500 nm and 2500 nm in the simulation and an average measured absorption of 85% in the spectrum of 500 nm–2300 nm. Our absorber offers a wide and smooth absorption spectrum with high absorption in both simulation and experiment, which can cover both the visible and infrared frequency ranges. We emphasize that our proposal is general and can be applied to further broaden the absorption bandwidth with more slow-wave structures integrated in a unit cell, allowing for realization of thin film thermal emitters and blackbody emission. In addition, these types of HMM absorbers are also promising candidates for improving the performance of thermo-photovoltaic systems.

3.1. Methods

3.1.1. Simulations

We performed the full wave simulations using Lumerical, a commercial FDTD software package. For the tapered strip absorber, the simulations are performed in two-dimensional layouts. In the simulations, the mesh grid was set to 5 nm over the entire simulation volume, with a refinement (1 nm) over the volume occupied by the tapered strips. A unit cell of the tapered strip is simulated using periodic boundary conditions along the x-axis and perfectly matched layers along the propagation of electromagnetic waves (z-axis). Plane waves were launched incident to the unit cell along the $+z$ direction with the electric field along the x direction, and reflection is monitored with a power monitor placed behind the radiation source; transmission is monitored with a power monitor placed behind the structure. Electric and magnetic fields are detected using the frequency profile monitors.

We used the three-dimensional layouts to simulate the quadrangular frustum pyramids absorber. In the simulations, for the volume occupied by the pyramids, the mesh grid was set to 8 nm along the x and y directions, and 2 nm along the z direction. A cubic mesh with a mesh size of 10 nm was employed for the other volume. We used periodic boundary conditions along the x and y-axes, and perfectly matched layers along the propagation of electromagnetic waves (z-axis). We also used power monitors to acquire the reflection and transmission, and frequency profile monitors to record the field profiles.

Optical constants of Al_2O_3, Al and Au were taken from Ref. [26].

3.1.2. Fabrication

The fabrication of the multilayered films started with a 100 nm Au film deposited on a flat silicon substrate using sputtering at a deposition rate of 0.5 nm/s. The fabrication process was followed by depositing 10 pairs of alternating Al_2O_3 (16 nm)/Al (24 nm) thin layers onto the Au film using sputtering. The film growth rates for Al_2O_3 and Al were 0.04 nm/s and 0.3 nm/s, respectively.

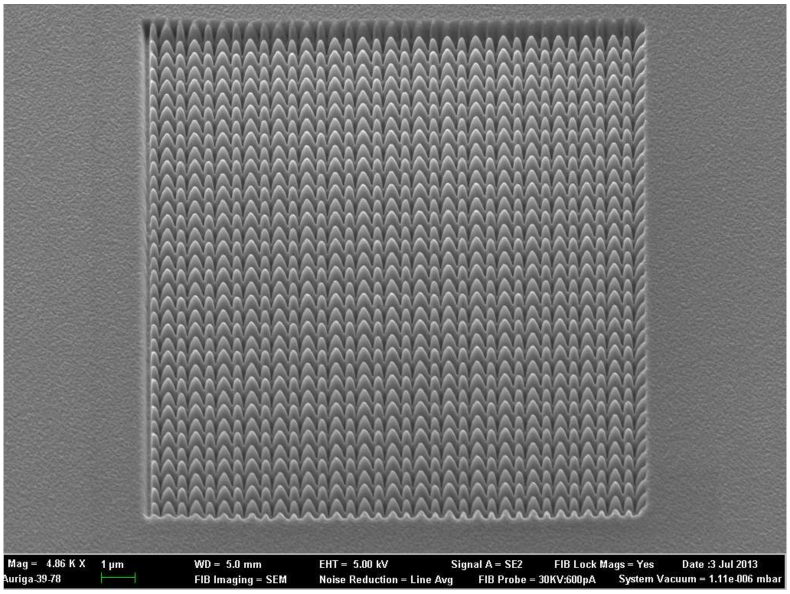

Figure 7. SEM images of 2D QFP arrays with square border (fabricated on 3 July 2013, as indicated at the right-bottom corner; the publication was very much delayed due to the experimental set-up for the long-wavelength measurement and some other reasons).

Arrays of HMM absorbers were fabricated using a cross-beam system (FIB and scanning electron microscope), where a constant current (20–50 pA) of Ga+ ions was focused onto the surface at normal incidence, with the position of the beam controlled by a lithography system. To fabricate the tapered strip array, during the FIB milling, we have used the grayscale bitmaps to pattern the nano-structure in order to precisely control the tapered angle. Assigning a bitmap to a shape is equivalent to varying the dose pixel by pixel using the grayscale intensity as a weight, and the dose is then distributed over the shape as a function of the brightness of the pixel. With the carefully designed grayscale bitmap and proper doses, we have successfully fabricated the 1D tapered strip arrays with optimized parameters.

For 2D QFP arrays, we first fabricated the 1D tapered strip array and then milled the orthogonally oriented strip array. To compensate for the structural anisotropy caused by milling orthogonally oriented strips, we have adjusted the grayscale bitmaps and dose value. Figure 7 shows the SEM images of 2D QFP arrays with the square border.

3.1.3. Optical Measurements

Reflection spectra of the fabricated samples were studied using two different systems. In the wavelength range of 500 nm–1650 nm, we use a homemade linear reflection spectroscopy to measure the reflection. The spectroscopic setup included an IX71 microscope (Olympus) equipped with a super-continuum white light laser source (NKT) and fiber-coupled spectrometers. The reflected light was collected in the backscattering configuration using an MPlanFL (Olympus) objective with a magnification of ×100 (numerical aperture (N.A.) = 0.8). A tunable pinhole with a minimum diameter of 1000 µm is set at the conjugate plane of the sample to control the image area with a diameter of 10 µm. In this way, we can make sure that the backscattering light collected is mainly from the sample area and therefore suppresses the background noise. The signal was measured by using an Ocean Optics USB2000 spectrometer at the visible frequency (350–1000 nm) and by using an Ocean Optics NIR-QUEST spectrometer in the near-infrared range (900–1700 nm). In the long wavelength range (above 1750 nm), we adopt another detection system. An inverted microscope (Ti-u from Nikon), followed by a confocal optical path, collects signals into a monochromator (SP 2300i from Princeton Instruments). An infrared detector (Zolix) is used to measure the spectrum when the monochromator is scanning. Additionally, a long pass filter (for the wavelength above 1750 nm) is used to block shorter wavelengths for the monochromator. Reflectivity spectra were obtained by using calibration reflection measurements with a reference broadband dielectric mirror that exhibits an average reflection of 99% between 400 and 700 nm of light wavelengths. In the wavelength range above 700 nm, we used the gold film as the reference mirror.

ACKNOWLEDGMENT

The authors are grateful to useful discussions with Drs. Yi Jin and Yanxia Cui. This work is partially supported by the National High Technology Research and Development Program (863 Program) of China (No. 2012AA030402) and the National Natural Science Foundation of China (Nos. 91233208 and 61178062), and Swedish VR grant (# 621-2011-4620).

REFERENCES

1. Watts, C. M., X. L. Liu, and W. J. Padilla, "Metamaterial electromagnetic wave absorbers," *Adv. Mater.*, Vol. 24, OP98–OP120, 2012.
2. Kraemer, D., et al., "High-performance flat-panel solar thermoelectric generators with high thermal concentration," *Nat. Mater.*, Vol. 10, 532–538, 2011.
3. Rephaeli, E. and S. H. Fan, "Absorber and emitter for solar thermo-photovoltaic systems to achieve efficiency exceeding the Shockley-Queisser limit," *Opt. Express*, Vol. 17, 15145–15159, 2009.
4. Teperik, T. V., et al., "Omnidirectional absorption in nanostructured metal surfaces," *Nat. Photon.*, Vol. 2, 299–301, 2008.
5. Bonod, N., G. Tayeb, D. Maystre, S. Enoch, and E. Popov, "Total absorption of light by lamellar metallic strips," *Opt. Express*, Vol. 16, 15431–15438, 2008.

6. Kravets, V. G., F. Schedin, and A. N. Grigorenko, "Plasmonic blackbody: Almost complete absorption of light in nanostructured metallic coatings," *Phys. Rev. B*, Vol. 78, 205405, 2008.
7. Hibbins, A. P., et al., "Resonant absorption of electromagnetic fields by surface plasmons buried in a multilayered plasmonic nanostructure," *Phys. Rev. B*, Vol. 74, 073408, 2006.
8. Le Perchec, J., P. Quemerais, A. Barbara, and T. Lopez-Rios, "Why metallic surfaces with grooves a few nanometers deep and wide may strongly absorb visible light," *Phys. Rev. Lett.*, Vol. 100, 066408, 2008.
9. White, J. S., et al., "Extraordinary optical absorption through subwavelength slits," *Opt. Lett.*, Vol. 34, 686–688, 2009.
10. Landy, N. I., S. Sajuyigbe, J. J. Mock, D. R. Smith, and W. J. Padilla, "A perfect metamaterial absorber," *Phys. Rev. Lett.*, Vol. 100, 207402, 2008.
11. Tao, H., et al., "A metamaterial absorber for the terahertz regime: Design, fabrication and characterization," *Opt. Express*, Vol. 16, 7181–7188, 2008.
12. Liu, X. L., T. Starr, A. F. Starr, and W. J. Padilla, "Infrared spatial and frequency selective metamaterial with near-unity absorbance," *Phys. Rev. Lett.*, Vol. 104, 207403, 2010.
13. Liu, N., M. Mesch, T. Weiss, M. Hentschel, and H. Giessen, "Infrared perfect absorber and its application as plasmonic sensor," *Nano Lett.*, Vol. 10, 2342–2348, 2010.
14. Ye, Y. Q., Y. Jin, and S. L. He, "Omnidirectional, polarization-insensitive and broadband thin absorber in the terahertz regime," *J. Opt. Soc. Am. B*, Vol. 27, 498–504, 2010.
15. Liu, X. L., et al., "Taming the blackbody with infrared metamaterials as selective thermal emitters," *Phys. Rev. Lett.*, Vol. 107, 045901, 2011.
16. Cui, Y. X., et al., "A thin film broadband absorber based on multi-sized nanoantennas," *Appl. Phys. Lett.*, Vol. 99, 253101, 2011.
17. Huang, L., et al., "Experimental demonstration of terahertz metamaterial absorbers with a broad and flat high absorption band," *Opt. Lett.*, Vol. 37, 154–156, 2012.
18. Aydin, K., V. Ferry, R. M. Briggis, and H. A. Atwater, "Broadband polarization-independent resonant light absorption using ultrathin plasmonic super absorbers," *Nat. Commun.*, Vol. 2, 517, 2011.
19. Kravets, V. G., S. Neubeck, and A. N. Grigorenko, "Plasmonic blackbody: Strong absorption of light by metal nanoparticles embedded in a dielectric matrix," *Phys. Rev. B*, Vol. 81, 165401, 2010.
20. Hedayati, M. K., et al., "Design of a perfect black absorber at visible frequencies using plasmonic metamaterials," *Adv. Mater.*, Vol. 23, 5410–5414, 2011.
21. Rephaeli, E. and S. H. Fan, "Tungsten black absorber for solar light with wide angular operation range," *Appl. Phys. Lett.*, Vol. 92, 211107, 2008.
22. Søndergaard, T., et al., "Plasmonic black gold by adiabatic nanofocusing and absorption of light in ultra-sharp convex grooves," *Nat. Commun.*, Vol. 3, 969, 2012.
23. Cui, Y. X., et al., "Ultrabroadband light absorption by a sawtooth anisotropic metamaterial slab," *Nano Lett.*, Vol. 12, 1443–1447, 2012.
24. Ding, F., Y. X. Cui, X. C. Ge, Y. Jin, and S. L. He, "Ultra-broadband microwave metamaterial absorber," *Appl. Phys. Lett.*, Vol. 100, 103506, 2012.
25. Elser, J., R. Wangberg, V. A. Podolskiy, and E. E. Narimanov, "Nanowire metamaterials with extreme optical anisotropy," *Appl. Phys. Lett.*, Vol. 89, 261102, 2006.
26. Palik, E. D., *Handbook of Optical Constants of Solids,* Academic Press, New York, 1998.
27. Born, M. and E. Wolf, *Principle of Optics,* 6th Edition, Macmillan, New York, 1964.
28. He, J. L. and S. L. He, "Slow propagation of electromagnetic waves in a dielectric slab waveguide with a left-handed material substrate," *IEEE Microw. Wirel. Compon. Lett.*, Vol. 16, 96–98, 2006.
29. He, S. L., Y. R. He, and Y. Jin, "Revealing the truth about 'trapped rainbow' storage of light in metamaterials," *Sci. Rep.*, Vol. 2, 583, 2012.